Geophysical Journal International

Geophys. J. Int. (2026) **246,** 1–17
Advance Access publication 2026 April 30
Research paper

https://doi.org/10.1093/gji/ggag142

Q estimation and generalization of the Battaglia–Aki method

Ayman N. Qadrouh,[1] José M. Carcione,[2,3] Mamdoh Alajmi [1] and Jing Ba[3]

[1]*KACST, PO Box 6086, Riyadh 11442, Saudi Arabia. E-mail: malajmi@kacst.gov.sa*
[2]*Istituto Nazionale di Oceanografia e di Geofisica Sperimentale (OGS), Borgo Grotta Gigante 42c, 34010 Sgonico, Trieste, Italy*
[3]*School of Earth Science and Engineering, Hohai University, Nanjing 211100, China*

Accepted 2026 April 3. Received 2026 March 2; in original form 2025 December 23

SUMMARY

The intrinsic attenuation of a seismic wave is a key property of rocks. Knowledge of *Q* (quality factor), which measures the attenuation, provides information not only about the type of rock, but above all about the pore fluids. In addition, the attenuation is needed for inverse *Q* filtering and is useful for localizing seismic sources. The methods for determining *Q* are based on the amplitude and frequency content of the signal, for example, the spectral ratio and frequency shift methods. In this paper, we consider a nearly frequency-independent *Q* factor so that the attenuation factor is proportional to frequency, so that high frequencies are attenuated. We use the frequency shifts (from the source to the receiver) to estimate the *Q*-factor for media with arbitrary geometric interfaces. The amplitude can be affected by factors other than attenuation, namely, geometric spreading and transmission coefficient. The shifts depend on the type of spectrum, which differs for seismic, microseismic and seismological (earthquake) sources. The inversion for *Q* assumes that the source spectrum is known, as well as the seismic velocities and the location of the interfaces and the source. On the other hand, if *Q* is known, sources can be located based on a generalization of the Battaglia–Aki method to heterogeneous media and using the centroid of the spectrum and the traveltimes at the receivers instead of the amplitude of the signal in the time domain. Alternatively, we provide formulas for the maximum of the signal spectrum that can also be used (peak frequency shift). Modelling and inversion is performed with 2-D and 3-D ray tracing algorithms based on Fibonacci search and minimizations with the Praxis algorithm and simulated annealing. We generate synthetic test seismograms with a direct 2-D full-wave algorithm based on the pseudo-spectral Fourier method, compare the results with those of ray tracing and use the minimization algorithm in combination with ray tracing to determine the source location.

Key words: Numerical modelling; Acoustic properties; Seismic attenuation; Wave propagation.

1 INTRODUCTION

The quality factor *Q* is a dimensionless measure of the energy loss per cycle of a wave field, and a proper understanding of this factor is important in a variety of fields, from seismology to geophysical prospecting to the electrical sciences (J.M. Carcione et al. 2024a). J.M. Carcione et al. (2024b) have recently provided an overview of the physics related to the quality factor for different rheologies.

The attenuation is useful to obtain information about the rock formations (permeability, fluid type, porosity, saturation, etc.) (e.g. J.M. Carcione & S. Picotti 2006; F. Cavallini et al. 2017), to improve the resolution of standard imaging techniques by applying an inverse *Q* filter (Z. Chen et al. 2014) or to localize seismic sources (J. Battaglia & K. Aki 2003; H. Kumagai et al. 2010; T. Permana et al. 2020). Microseismicity due to fluid injection, hydraulic fracturing, volcanic shaking or earthquakes are different cases involving different sources whose spectra have well-defined characteristics. In all these cases, the frequency shift method can be used to estimate *Q*. It has been shown to be the most reliable method when the signal-to-noise ratio is low (S. Picotti & J.M. Carcione 2006).

In seismic exploration, sources can be located using a reverse-time migration algorithm based on a dispersionless anelastic rheology by back-propagating the recorded field with a negative quality factor (J.M. Carcione & B. Ursin 2016). It is based on a wave equation for anelastic media in which the phase velocity is frequency-independent. In the migration process, the recorded seismogram is used as a time-dependent boundary condition. The seismic trace is applied at each receiver in reverse time, and the propagation goes back in time to the origin time where the best focusing occurs, so the sources are mapped in this way. In seismology, there are two main methods to localize the source of an earthquake: Triangulation is used to draw circles centred at the receivers with radii corresponding to distances calculated from the *P* and *S* traveltimes (M. Båth 1979). The point where all circles intersect is the location of the epicentre of the earthquake. On the other hand, transmission traveltime tomography is used to find the hypocentre (e.g. A. Michelini & T.V. McEvilly 1991).

In this work, quality factors are determined using a ray tracing technique based on the Fibonacci search (L. Onnis & J.M. Carcione 2017) and measured frequency shifts at the receivers, knowing the location of the source at depth. Once the quality factor has been determined, sources can be localized. In particular, J. Battaglia & K. Aki (2003) used a simple analytical equation to calculate the amplitude decay from the source location (a volcanic tremor) to the receiver. A similar, although not identical, method was proposed by H. Kumagai et al. (2010). In both cases, the medium is assumed to be homogeneous. However, in realistic situations, the medium is heterogeneous and a numerical algorithm is required. The proposed ray tracing algorithm, which takes into account the attenuation and transmission losses, is sufficiently efficient for this purpose.

The problem at hand considers the response of seismic sources located at depth, whose wavefield is recorded at the surface. We focus on direct arrivals since multiples have a lower amplitude and are difficult to pick and detect. Instead of the amplitude of the signal (J. Battaglia & K. Aki 2003, eq. 9), we use the centroid of the spectrum at the surface to define the objective function, that is, we adopt the frequency-shift method of Y. Quan & J.M. Harris (1997). In addition, we generate synthetic seismograms in viscoacoustic media with an almost constant Q, without any approximation, using the Fourier pseudospectral method (J.M. Carcione et al. 1988; J.M. Carcione 2022) and compare results to those of the ray tracing algorithm.

2 PROPAGATION IN HOMOGENEOUS MEDIA

Let us assume that the spectrum of the signal at a receiver very close to the source location (hereafter source) can be represented by a Ricker wavelet,

$$s(t) = (1 - 2a^2)\exp(-a^2), \quad a = \pi f_0(t - t_s), \tag{1}$$

where f_0 is peak frequency and we take $t_s = 1.4/f_0$. Its spectrum is

$$S(f) = \frac{2\bar{a}^2}{\sqrt{\pi}}\exp(-\bar{a}^2 - \mathrm{i}\omega t_s), \quad \bar{a} = \frac{\omega}{\omega_0} = \frac{f}{f_0}. \tag{2}$$

where f is the frequency and $\omega = 2\pi f$ is the angular frequency (J.M. Carcione et al. 2015). The centroid is

$$f_{c0} = \frac{\displaystyle\int_0^\infty f|S(f)|\mathrm{d}f}{\displaystyle\int_0^\infty |S(f)|\mathrm{d}f} = \frac{2}{\sqrt{\pi}} f_0 = 1.1284 f_0. \tag{3}$$

(I.S. Gradshteyn & I.M. Ryzhik 2007, eq. 3.326 (2)).

The propagation at a distance r is affected by intrinsic attenuation and the spectrum at the receiver is

$$R(f) = gS(f)\exp[-\alpha(f)r] = gS(f)\exp(-t_r f), \quad t_r = \frac{\pi r}{vQ} \tag{4}$$

(e.g. J. Battaglia & K. Aki 2003), where g is a geometrical spreading factor (g=1 in 1-D and $1/r$ in 3-D), Q is the quality factor,

$$\alpha \approx \frac{\pi f}{vQ} \tag{5}$$

is the attenuation factor ($Q \gg 1$) and v is the phase velocity. In the examples below, we consider a nearly-constant Q (J.M. Carcione 2022, section 2.4.5), with five Zener elements, such that Q is almost constant with frequency around the peak of the source spectrum. If Q is assumed constant over all frequencies and velocity dispersion is neglected (v is frequency independent), the maximum amplitude of the function R at a distance r is located at

$$f_p = f_0\left(\sqrt{1 + b^2} - b\right), \quad b = \frac{t_r f_0}{4}, \tag{6}$$

and the centroid is given by

$$f_c = \frac{\displaystyle\int_0^\infty f|R(f)|\mathrm{d}f}{\displaystyle\int_0^\infty |R(f)|\mathrm{d}f}, \tag{7}$$

which is computed numerically (I.S. Gradshteyn & I.M. Ryzhik 2007, eq. 3.462 (1)). The centroid frequency can also be obtained as the instantaneous frequency at the peak of the signal envelope. The instantaneous frequency is the time derivative of the phase of the complex trace, which is a complex continuation of the real trace, where the imaginary part is the Hilbert transform of the real signal. The complex trace in exponential form basically separates amplitude (envelope) from phase (e.g. J.M. Carcione et al. 2021; J.M. Carcione 2022, section 2.12).

Defining the frequency shift based on the initial peak frequency as

$$\Delta f_p = f_0 - f_p, \tag{8}$$

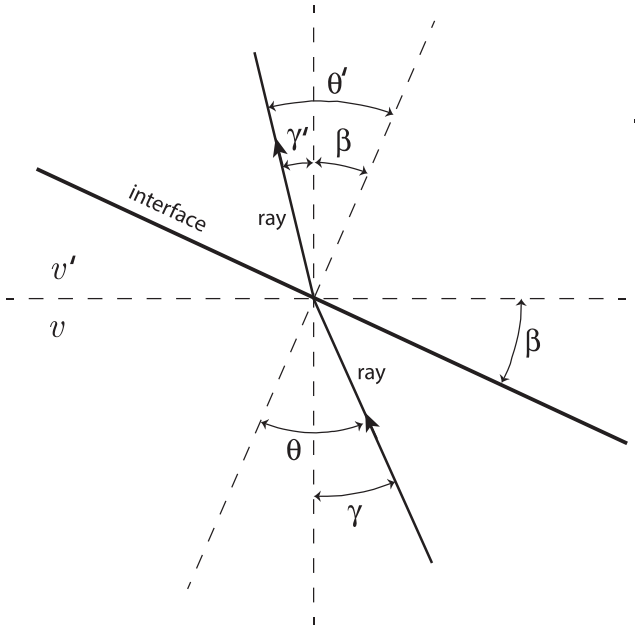

Figure 1. Transmission of a ray at an interface.

we obtain, from the equation of the maximum of function R above,

$$Q = \frac{\pi r f_0}{2v}\left(\frac{f_0}{f_p} - \frac{f_p}{f_0}\right)^{-1} = \frac{\pi r f_0 (f_0/\Delta f_p - 1)}{2v(2 - \Delta f_p/f_0)}. \tag{9}$$

In terms of the centroid, the frequency shift is

$$\Delta f_c = f_{c0} - f_c = 1.1284 f_0 - f_c. \tag{10}$$

The method of J. Battaglia & K. Aki (2003) can be used to locate sources after Q has been obtained. We generalize this method to heterogeneous media in the next section.

3 PROPAGATION IN HETEROGENEOUS MEDIA

Assume a medium composed of N geological interfaces and viscoacoustic propagation (P waves). Each layer is isotropic, anelastic and homogeneous and characterized by its acoustic velocity, quality factor and mass density. The interfaces can have any geometrical shape provided that they do not cross each other (e.g. pinchouts are not allowed) and extend from one side of the model to the other. They are defined by a small number (∼5) of equi-spaced starting points along the horizontal direction (x-variable). Spline interpolation between the starting points is performed at a more densely sampled set of equi-spaced points (∼2000). The larger set of points is connected by line segments. Receivers are located on the surface.

With the geological model defined in the (x, z)-plane, we consider a ray departing from the source, making an angle γ with the vertical z-axis (see Fig. 1). Because each layer is isotropic and homogeneous, the ray follows a straight path until it intersects an interface. Each interface is composed of a large number of segments. To determine where an intersection between the ray and an interface occurs, the algorithm loops over all the segments of an interface. The transmission at a given interface is illustrated in Appendix A.

Energy is also lost at interfaces, where we discard transmitted rays that exceed the critical angle. The loss by transmission at each interface involves the transmissivity corresponding to the stress (or pressure) field, given by

$$\mathcal{T} = \sqrt{\frac{Z\cos\theta'}{Z'\cos\theta}}\,T, \qquad T = \frac{2Z'\cos\theta}{Z'\cos\theta + Z\cos\theta'}, \tag{11}$$

where $Z(f) = \rho v(f)$ is the impedance, ρ is the mass density, θ is the ray angle with respect to a line perpendicular to the interface and v and v' depend on frequency f. Primed quantities correspond to the transmission medium. Eqs (11) result from eqs (8.184) and (8.158) in J.M. Carcione (2022) and a mathematical analogy between *SH* and *P* waves, considering that the acoustic stress field is mathematically equivalent to the displacement of *SH* waves (see appendix B in L. Onnis & J.M. Carcione 2017). Note that the transmission coefficient corresponding to the displacement field has a different expression (e.g. E.A. Robinson & S. Treitel 1980, pp. 296–329). For brevity, appendix B gives a demonstration for 1-D media. Here we consider the stress field since this field is recorded at the receivers in the full-wave simulation below. Eqs (11) are supplemented with Snell's law: $\sin\theta/v = \sin\theta'/v'$ (J.M. Carcione 2022; L. Onnis & J.M. Carcione 2017). Both $\mathcal{T}$ and the Snell law depend on frequency through the phase velocities, but we neglect inhomogeneous body waves for

which the propagation and attenuation directions differ; here we consider homogeneous waves (see J.M. Carcione & B. Ursin 2016, eq. 7; J.M. Carcione 2022, eq. 3.27, fig. 3.1 and section 3.5).

Moreover, the signal decays by geometrical spreading. In 3-D media, the decay is proportional to $1/r$, that is, a pulse with amplitude 1 at the source location ($r_0 = 1$ m) will decay to $1/(r/r_0)$ ($r \geq r_0$) at a distance r from the source. Then, the total amplitude spectrum from the source to the surface receiver in 3-D is given by

$$R(f) = \frac{\prod_{j=1}^{N} \mathcal{T}_j(f)}{r_0^{-1} \sum_{k=1}^{N+1} r_k} S(f) \prod_{i=1}^{N+1} \exp(-\alpha_i r_i) = \frac{\prod_{j=1}^{N} \mathcal{T}_j(f)}{r_0^{-1} \sum_{k=1}^{N+1} r_k} S(f) \exp\left(-\pi f \frac{T_N}{\bar{Q}_N}\right) \tag{12}$$

where r_i is the length of the ray in medium i ($\sum r_k \geq r_0$), $S(f)$ is given by eq. (2),

$$\bar{Q}_N = T_N \left(\sum_{i=1}^{N+1} \frac{t_i}{Q_i} \right)^{-1}, \quad \text{with} \quad T_N = \sum_{i=1}^{N+1} t_i, \quad t_i = \frac{r_i}{v_i}, \tag{13}$$

is the average Q from the source to the receiver, the so-called Wyllie Q in A.N. Qadrouh et al. (2017) [the 3-D kernel $|\exp(-\mathrm{i}\omega r_i/v_{\mathrm{ci}})| = \exp(-\alpha_i r_i)$, with $\alpha_i = -\omega \mathrm{Im}(1/v_{ci}) \approx \pi f/(v_i Q_i)$ for $Q \gg 1$ (e.g. J.M. Carcione 2022, eqs 2.126), where v_{ci} are the complex velocities of each layer].

Eq. (12) is the generalization of eqs (4) and (8) of J. Battaglia & K. Aki (2003) to inhomogeneous media. Eq. (12) is acceptable, since comparisons with full-wave simulations show a very good agreement (L. Onnis & J.M. Carcione 2017). In homogeneous media (without interfaces), eq. (12) becomes

$$R(f) = \frac{S(f)}{(r/r_0)} \exp\left(-\frac{\pi f r}{v Q}\right), \tag{14}$$

where r is the source–receiver distance.

In 2-D space, the exponential kernel in eq. (12) must be replaced by the zero-order Hankel function of the second kind $H_0^{(2)}$, which also contains the geometrical spreading factor proportional to $1/\sqrt{r}$. For large arguments, the exact Hankel function can be replaced by its asymptotic expression: $H_0^{(2)}(z) = \sqrt{2/(\pi z)} \exp[\mathrm{i}(-z + \pi/4)]$, $(z = \omega r/v_{\mathrm{c}})$ (F. Mainardi 2022, eq. B.24). We consider an average complex velocity from source to receiver given by the time-average equation,

$$v_{\mathrm{c}} = r \left(\sum_{k=1}^{N+1} \frac{r_k}{v_{ck}} \right)^{-1}, \quad r = \sum r_k \tag{15}$$

or, alternatively, defining an average complex modulus $\rho v^2 (1 + \mathrm{i}/\bar{Q}_N)$,

$$v_{\mathrm{c}} = v \sqrt{1 + \frac{\mathrm{i}}{\bar{Q}_N}}, \quad v = r \left(\sum_{k=1}^{N+1} \frac{r_k}{v_k}, \right)^{-1} = \frac{r}{T_N}, \tag{16}$$

where v is an average phase velocity. It can be shown that eqs (15) and (16) are approximately equal for low-loss media ($Q \gg 1$), and that these effective complex velocities are good approximation also in 3-D space. Then

$$R(f) \approx \omega S(f) H_0^{(2)}(\omega r/v_{\mathrm{c}}) \prod_{j=1}^{N} \mathcal{T}_j(f), \tag{17}$$

(J.M. Carcione 2022, section 3.6). In the homogeneous case:

$$R(f) = \omega S(f) H_0^{(2)}(\omega r/v_{\mathrm{c}}). \tag{18}$$

The ω factor multiplying the source spectrum is due to the fact that in the simulation below we compute the stress field and we add the source as a time derivative (see eq. F3).

To obtain synthetic seismograms, $u(t)$, we multiply R in eq. (12) by the phase factor of the total traveltime,

$$\bar{u}(f) = R(f) \exp(-2\mathrm{i}\pi f T_N) \tag{19}$$

and compute a Fourier transform to the time domain.

A rough approximation of the peak frequency shift is

$$\Delta f_{\mathrm{p}} = f_0 - (f_0^2/4) \left(\sqrt{t_{\mathrm{r}}^2 + 16/f_0^2} - t_{\mathrm{r}} \right), \tag{20}$$

where

$$t_{\mathrm{r}} = \frac{\pi T_N}{\bar{Q}_N}. \tag{21}$$

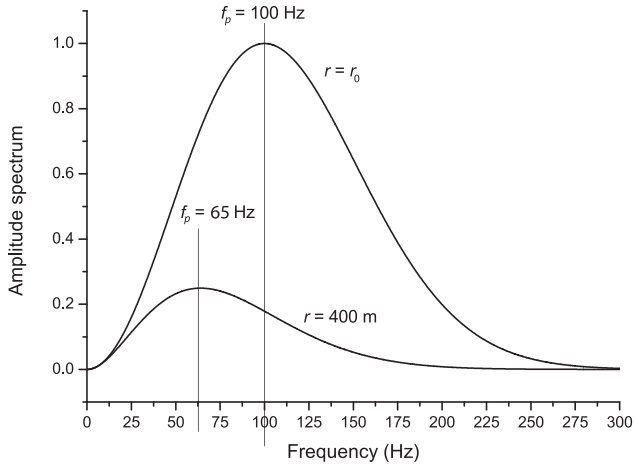

Figure 2. Amplitude spectra $|R(f)|$ at the source and receiver, where f_p is the frequency at the maximum.

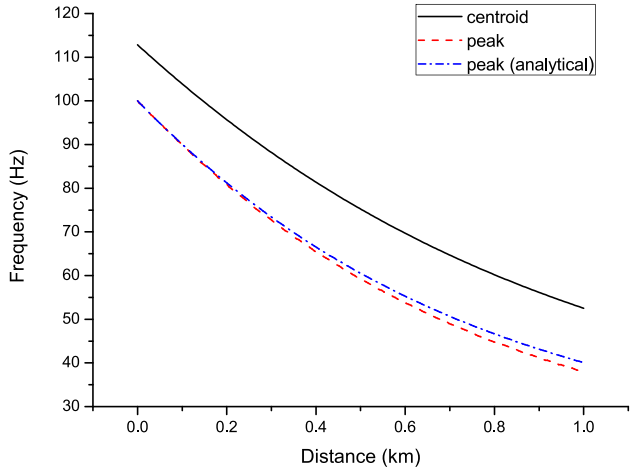

Figure 3. Centroid (f_c) and peak (f_p) frequency of the spectrum as a function of distance.

with $\bar{Q}_N$ given in eq. (13). It can be shown that

$$\bar{Q}_N = \frac{\pi T_N f_0 (f_0/\Delta f_\mathrm{p} - 1)}{2(2 - \Delta f_\mathrm{p}/f_0)}. \tag{22}$$

A more precise evaluation of the final peak frequency is $f_\mathrm{p}(J)$, where

$$\begin{aligned} f_\mathrm{p}(1) &= f_0 \left(\sqrt{1+b^2} - b\right), \quad b = \frac{\pi t(1) f_0}{4Q(1)}, \quad j = 1, \\ f_\mathrm{p}(j) &= f_\mathrm{p}(j-1) \left(\sqrt{1+b^2} - b\right), \quad b = \frac{\pi t(j) f_\mathrm{p}(j-1)}{4Q(j)}, \quad j \geq 2 \end{aligned} \tag{23}$$

where $j = 1$ is the medium where the source is located (the lower medium), and $j = J$ corresponds to the shallower medium. Then,

$$\Delta f_\mathrm{p} = f_0 - f_\mathrm{p}(J), \tag{24}$$

assuming the velocity and quality factor frequency independent, since this equation is based on eq. (6). On the other hand, the centroid shift is $1.1284 f_0 - f_\mathrm{c}$, where f_c is given by eq. (7), with R given by eqs (12) (for 3-D) or (17) (for 2-D).

The quality factors can be obtained by minimizing an objective function based on the frequency shifts. Assuming M receivers, such a function is

$$O(Q_i) = \sum_{m=1}^{M} |\Delta f_m - \Delta f_m(\mathrm{obs})|, \tag{25}$$

where Q_i are the quality factors of the layers, Δf_m are the computed centroid frequency shifts and Δf_m (obs) are the observed values. Alternatively, for flat horizontal interfaces, the quality factor can be obtained with the method outlined in Appendix C.

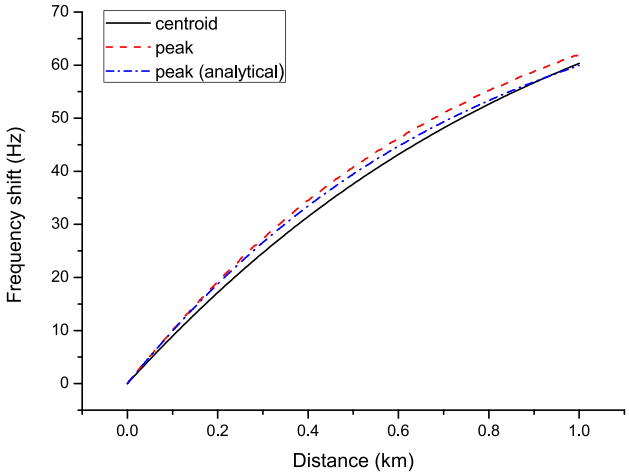

Figure 4. Centroid (Δf_c) and peak (Δf_p) frequency shifts as a function of distance.

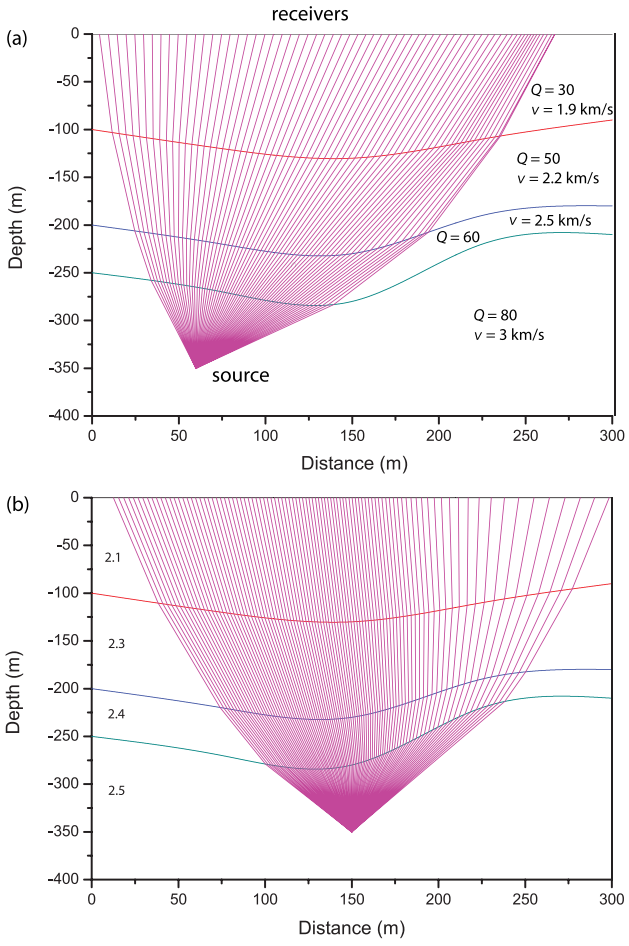

Figure 5. Ray paths traced from the source point at equi-spaced departures angles to a set of receivers at the surface, where $y_s = -350$ m, (a) $x_s = 60$ m and (b) $x_s = 150$ m. The smooth horizontal curves indicate the layer interfaces, Q is the quality factor and v is the acoustic high-frequency velocity. The numbers in panel (b) are the mass densities in g/cm^3. The rays correspond to the high-frequency (unrelaxed) velocity.

The location of the sources using the ray tracing method is outlined in Appendix D, which is a generalization of the method of J. Battaglia & K. Aki (2003) to the heterogeneous case. The rays at the receivers are obtained with the Fibonacci method (see Appendix E). To test the method, we invert data from the ray tracing algorithm and also from synthetic seismograms in anelastic media computed with the Fourier pseudospectral method to solve the differential equations given in J.M. Carcione et al. (1988) and Appendix F.

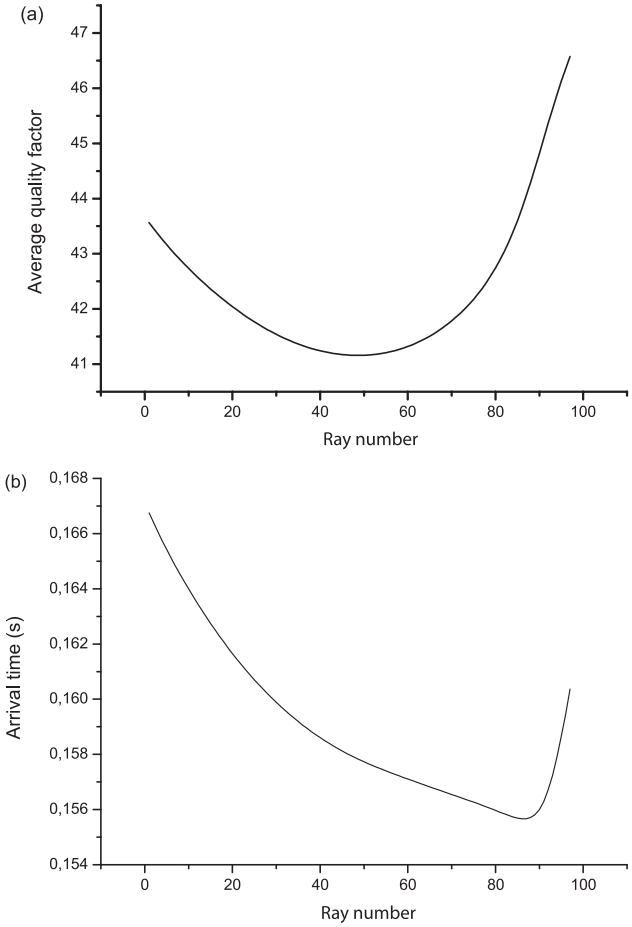

Figure 6. Average quality factor $\bar{Q}_N$ (a) and arrival time T_N (b) as a function of the receiver number, corresponding to Fig. 5(b).

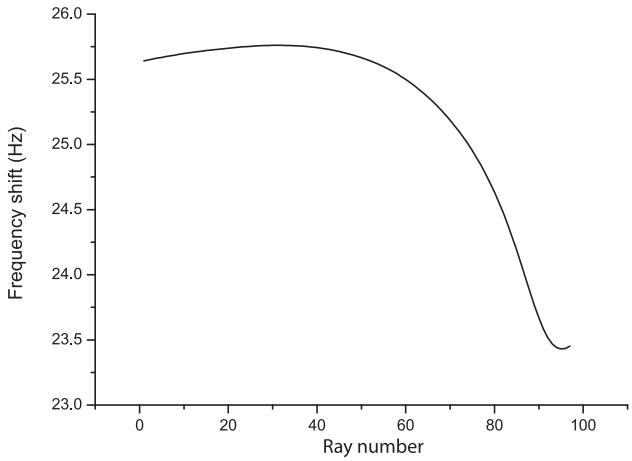

Figure 7. Frequency shifts (peak) as a function of the receiver number, corresponding to Fig. 5(b).

4 EXAMPLES

Let us first consider a homogeneous medium with $Q \approx 30$, $v_p = 2.5$ km s^{-1} (high-frequency limit or unrelaxed velocity), with five relaxation peaks equi-spaced in log(f) at $f_1 = 10$ Hz, $f_2 = 32$ Hz, $f_3 = 100$ Hz, $f_4 = 316$ Hz and $f_5 = 1000$ Hz, and a source peak frequency $f_0 = 100$ Hz. According to J.M. Carcione (2022, section 2.4.5), we obtain an almost constant quality factor at the source dominant frequency. Fig. 2 shows the spectra at the source and at a receiver located at $r = 400$ m, where the frequency at the maximum is indicated. Fig. 3 shows the centroid and peak frequency of the spectrum as a function of distance. The dashed red line corresponds

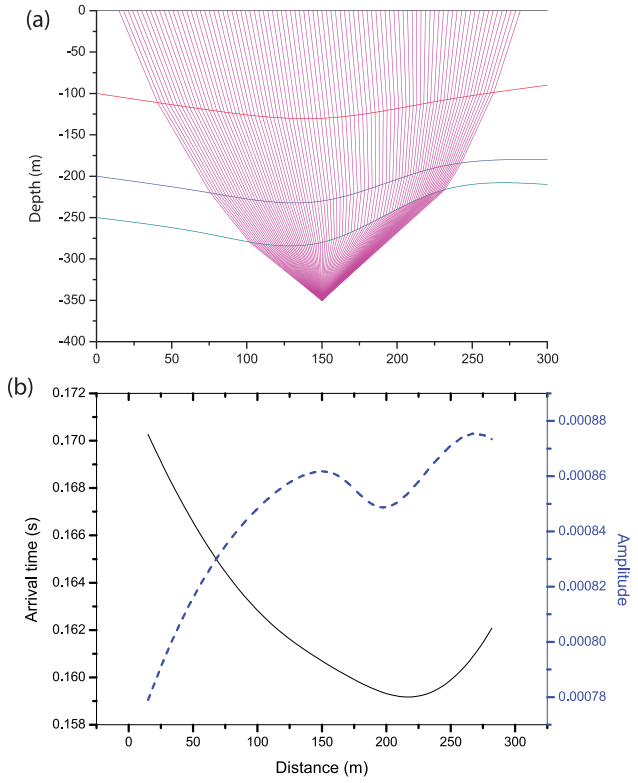

Figure 8. Ray paths from the source point to a set of equi-spaced receivers at the surface (a) and arrival time T_N and amplitudes at the receivers for a source of amplitude 1 (b), where $x_s = 150$ m. The Fibonacci search method is used to find the rays. The rays correspond to the high-frequency (unrelaxed) velocity. See Fig. 5 for the properties of each layer.

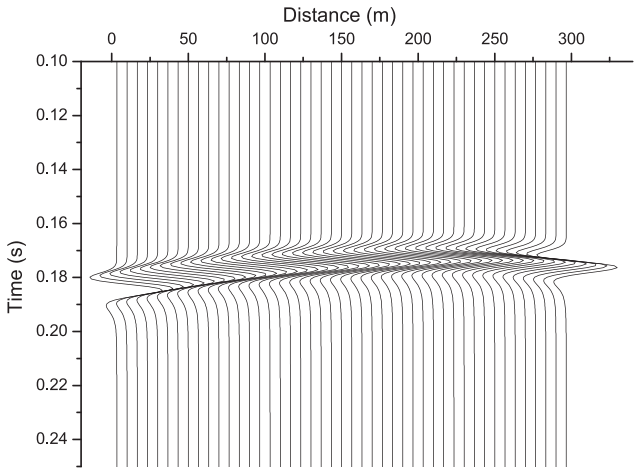

Figure 9. Seismogram corresponding to Fig. 8(a) obtained with 3-D ray tracing.

to the Zener model, where Q and v are frequency dependent in eq. (4). The blue dotted line (analytical, eq. 6) assumes Q frequency independent and considers the high-frequency velocity.

The centroid and peak frequency shifts (eqs 8 and 10) as a function of distance are shown in Fig. 4, from which it can be seen that they are very similar from a practical point of view. The centroid can then be used for the inversion, as this quantity is more robust than the frequency calculated at the maximum amplitude. Therefore, tracing rays and using the analytical formula (20) is consistent with frequency shifts based on the centroid of the signal.

Fig. 5 shows a 3-layer subsoil model, and the ray paths traced from two sources at equi-spaced departure angles. The source parameters of the previous example are assumed. In this case, we do not consider the Zener model, but a constant Q and velocity as indicated in Fig. 5(a). The numbers in Fig. 5(b) are the mass densities in g/cm^3. Fig. 6 shows the average quality factor $\bar{Q}_N$ (a) and arrival time T_N (b) (eq. 13) as a function of the number of rays at the surface, corresponding to Figs 5(b) and 7 represents the peak frequency shift.

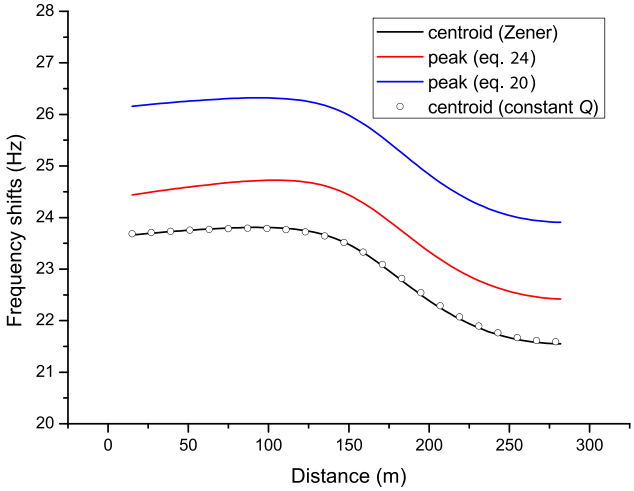

Figure 10. Peak frequency shifts [equations (20) (blue) and (24) (red)] and centroid shift (black) as a function of distance, corresponding to Fig. 8. The symbols correspond to Q and phase velocity frequency independent.

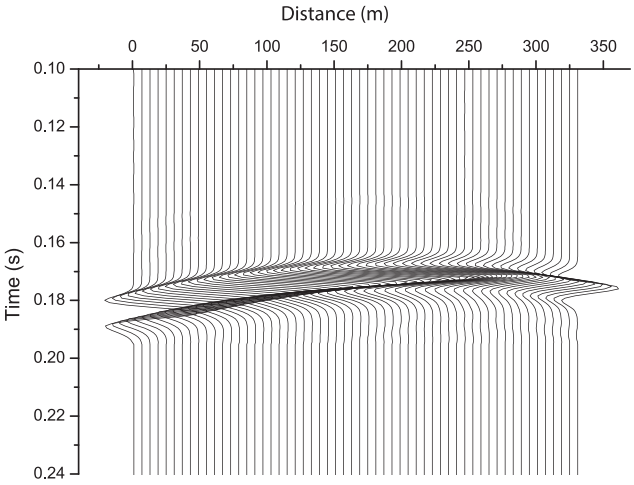

Figure 11. Seismogram of the stress field obtained using 2-D full-wave modelling. In this case, the medium is homogeneous and has the properties of the upper medium shown in Figs 5 and 8(a).

In a real experiment, we know the location of the receivers at the surface. The rays shown in Fig. 8(a) correspond to receivers equi-spaced at the surface. In these simulations, we have considered the Zener model to approximate the quality factor and velocity as a function of frequency. The rays in the figure correspond to a frequency of 100 Hz. Fig. 8(b) shows the amplitude (3-D, eq. 12) and arrival time (eq. 13) at the receivers for a source of amplitude 1 (single spike) for a frequency of 100 Hz.

The seismogram can be obtained from eq. (19) and a Fourier transform into the time domain. The FFT subroutine from the NASA LaRC Computer Manual, Vol. II Section E2.4 (1975) is used, which requires a complex vector of length a power of two. To obtain a real signal, we set $\bar{u}(f^-) = \bar{u}^*(f^+) = \text{conjg}[\bar{u}(f^+)]$, where the superscripts $+$ and $-$ denote positive and negative frequencies. The propagation of signals with a maximum frequency of $f_{\max} = 200$ Hz requires sampling rates smaller than $\mathrm{d}t = 1/(2f_{\max}) = 0.0025$ s to avoid aliasing problems. We use $2^9 = 512$ points and $\mathrm{d}t = 0.7$ ms. Fig. 9 shows the seismogram for 3-D space.

Fig. 10 shows the peak frequency shifts [Δf_{p} (eq. 20 at 100 Hz and eq. 24] and the centroid shift $1.1284 f_0 - f_{\mathrm{c}}$ (200 points have been used to discretize the spectrum). The symbols correspond to Q and the phase velocity frequency independent. As can be seen, the almost constant Q Zener model provides a good approximation to the constant Q.

Next, Q_i is inverted based on the centroid frequency shifts observed at the receivers in Fig. 8, where the geometric model, layer velocities and source location are known, by traveltime tomography and depth migration, for instance. The objective function is given by eq. (25), and the minimum is obtained using the Praxis algorithm explained in chapter 7 of R.P. Brent (1971). The geometry of the rays does not depend on Q and can be computed in the first iteration. With an initial guess $Q_i = 100$, 50 points to discretize the spectrum, a tolerance of 0.0119 and a maximum step size of 0.25, we obtain $Q_1 = 30.02$, $Q_2 = 49.2$, $Q_3 = 61.65$ and $Q_4 = 79.74$ (see the true values in Fig. 5a). We also minimize the objective function using a simulated annealing algorithm developed by W.L. Goffe et al. (1994), which is based on A. Corana et al. (1987). See A.N. Qadrouh et al. (2019) for examples of its application. The initial estimates

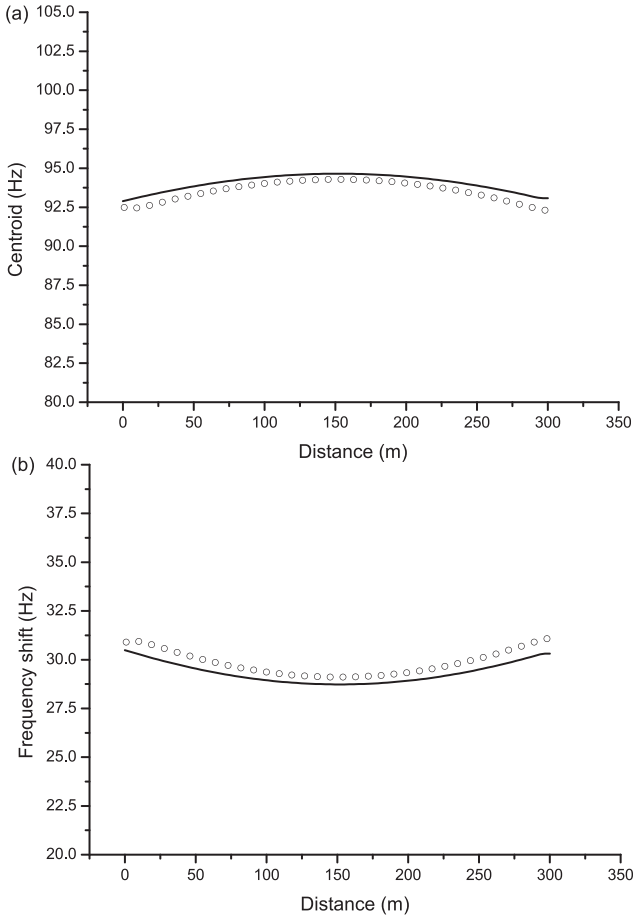

Figure 12. Centroids (a) and frequency shifts (b) at the receivers as a function of distance. The solid line and circles correspond to the 2-D theoretical (ray tracing) and numerical solutions, respectively. The medium is homogeneous with the properties of the upper medium (see Fig. 5).

to obtain the quality factors are $Q_i = 100$, with constraints between 5 and 200, 50 points to discretize the spectrum and the algorithm uses EPS = 1.0D-6, MAXEVL=10 000. We obtain $Q_1 = 29.99$, $Q_2 = 50.1$ $Q_3 = 59.59$ and $Q_4 = 79.95$.

The Praxis algorithm exhibits rapid, superlinear convergence near the minimum, performing as efficiently as gradient-based methods. It is particularly effective for well-behaved functions that are nearly quadratic, using quadratic approximation to minimize functions in a finite number of iterations. In contrast, simulated annealing has a slow, logarithmic rate of convergence to the global optimum, with 20 per cent more evaluations of the objective function compared to the Praxis algorithm, but it ensures avoidance of local minima.

We then show how to find the location of the source knowing the model by generalizing the technique of J. Battaglia & K. Aki (2003), that is, by minimizing the objective function (D2), where $\Delta f(\text{obs})$ and $T_N(\text{obs})$ are the observed centroid shifts and traveltimes at the receivers (with index m), respectively. This procedure requires more computer time than calculating the quality factors to obtain the result, as we need to calculate the rays using the Fibonacci algorithm for each iteration with different source locations. The Praxis algorithm with an initial guess: $(x_{s0}, y_{s0}) = (100, -300)$ m (71 m away from the real value), a tolerance of 0.2 and a maximum step size of 50, results in $(x_s, y_s) = (149.99, -350.00)$ m after a few iterations. With the simulated annealing algorithm, the same initial assumptions and the constraints (1, 300) and $(-400, -1)$ along the horizontal and vertical directions, the algorithm converges to the actual location.

Using the objective function (D2) implemented by J. Battaglia & K. Aki (2003) for homogeneous media, and based on root-mean-square (RMS) amplitudes, gives $(x_s, y_s) = (128, -320.00)$ m with the Praxis algorithm, which is far from the true value. Even in homogeneous media, the RMS criterion yields a higher error. This is because the average of RMS amplitudes is a rough approximation of the physical attenuation, unlike the ray tracing algorithm implemented here.

Finally, we generate data with a full-wave modelling code and compare results to those of the ray tracing. The synthetic seismograms are computed with a code based on a 2-D viscoacoustic stress–strain relation with five relaxation mechanisms ($L = 5$) based on Zener's mechanical model. The equations are given in Appendix F and result in a nearly constant Q. The algorithm is based on the pseudospectral Fourier method to calculate the spatial derivatives and a Runge–Kutta method of order 4 to recursively calculate the wave field in time. In this example, the source has an isotropic radiation pattern that is applied to the stress field. The grid has 715 ×

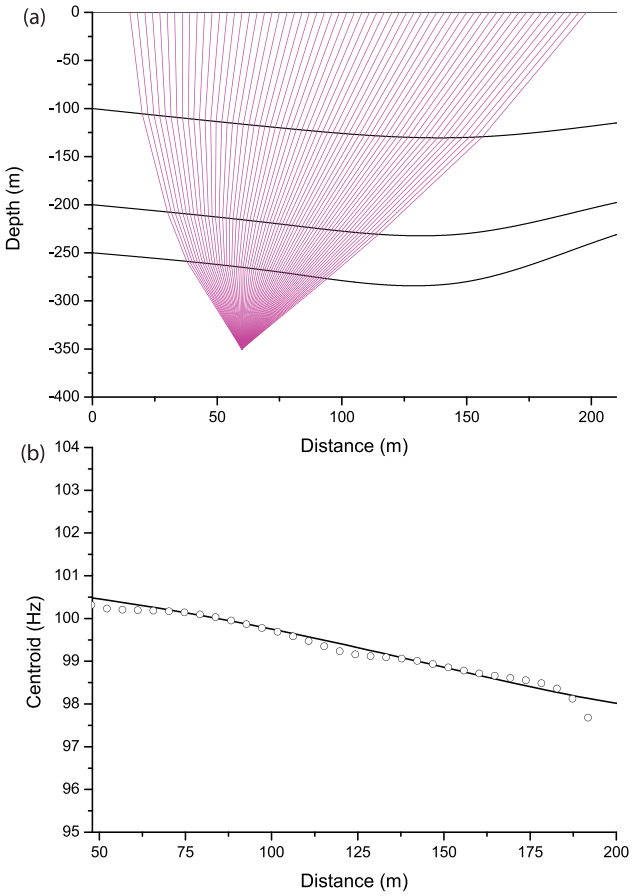

Figure 13. Geological model with rays (a) (see the properties of each layer in Fig. 5) and comparison between the ray (solid line) and full-wave (circles) centroids (b). The source is located at $(x_s,\ y_s) = (60,\ -350)$ m and the receivers between 25 and 200 m.

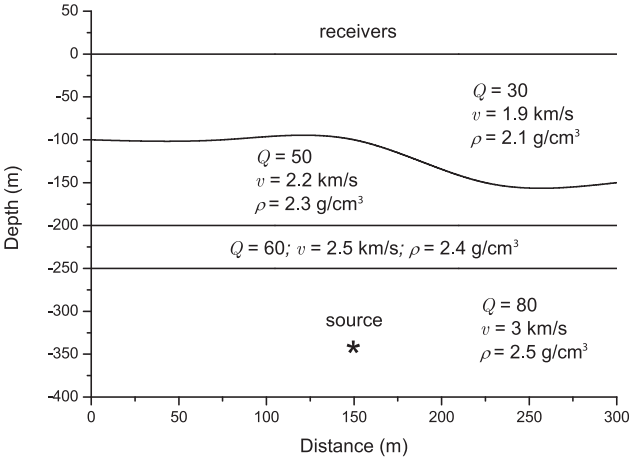

Figure 14. Geological model.

715 grid points, with the absorbing grid having 190 points on the sides, top and bottom. The cells are 0.9 m horizontally and vertically and the time step is 0.1 ms. To damp the diffractions caused by the discretization of the model, we use the method of X. Zeng & G.F. West (1996) with a smoothing factor of 0.2. The model is discretized in a finer mesh with 2861 grid points and then smoothed to the coarse mesh with 715 points. Fig. 11 shows the seismograms at the surface calculated with the full wave algorithm. In this case, the medium is homogeneous and has the properties of the upper medium ($v = 1.9$ km s^{-1}, $Q = 30$, $\rho = 2.1$ g cm^{-33}). Fig. 12 compares the

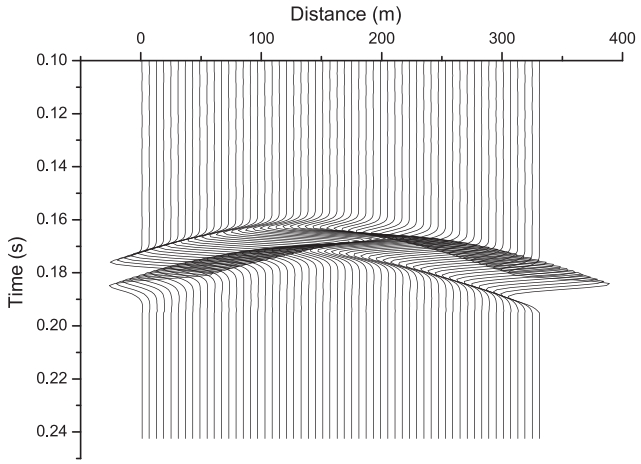

Figure 15. Seismogram corresponding to Fig. 14 (stress field) obtained with 2-D full-wave modelling.

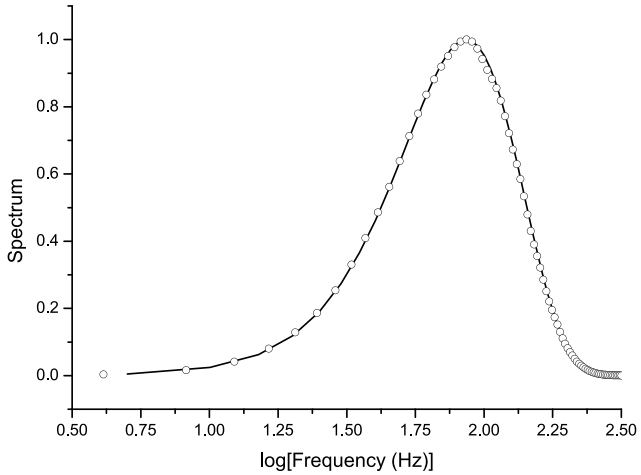

Figure 16. Normalized spectrum at a receiver located at $x = 225$ m in Fig. 14. The solid line and circles correspond to the theoretical (ray tracing) and numerical solutions, respectively.

corresponding centroids and frequency shifts as a function of distance x. The source centroid is

$$f_{c0} = \frac{\int_0^\infty f|fS(f)|\mathrm{d}f}{\int_0^\infty |fS(f)|\mathrm{d}f} = \frac{3}{4}\sqrt{\pi} f_0 = 133 \text{ Hz} \tag{26}$$

for $f_0 = 100$ Hz. Note that the spectrum of the original source (2) is multiplied by the frequency due to the time derivative in eq. (F1). When there is no attenuation, in 3-D space, the centroid at the receiver is the same as the centroid of the source (133 Hz). In 2-D space, the centroid is affected by the Hankel function, and instead of 133 Hz, it is 123.23 Hz, with $v = 3$ km s^{-1} and a distance of 100 m. The theoretical centroid of the field at the receivers is given by eq. (7), where R is given in eq. (18).

Fig. 13 shows the geological model and corresponding rays recorded at receivers between 25 and 200 m (a) and compares the centroids at these receivers computed with the ray tracing code (solid line) and full-wave simulation (circles). The agreement is satisfactory. Figs 14 and 15 show another geological model and the corresponding seismograms computed with the full-wave modelling code. Fig. 16 compares the normalized spectrum at the receiver located at $x = 225$ m, obtained with the ray tracing and grid method, showing that the ray tracing correctly describes the wave loss in the frequency domain. The centroids and centroid frequency shift are compared to those of the ray tracing in Fig. 17. The discrepancies can be due to the fact that the interfaces are not correctly described by the grid (the staircase effect produces diffractions), even if the Zeng and West smoothing is applied. We have also implemented the staggered-grid method (J.M. Carcione 1999, 2022, eq. 9.27) with no further improvement. Either the Praxis algorithm and simulating annealing converge to the source location. The input is the full wave seismogram (experimental data) and the algorithm uses the ray tracing to obtain the theoretical centroid frequency shifts.

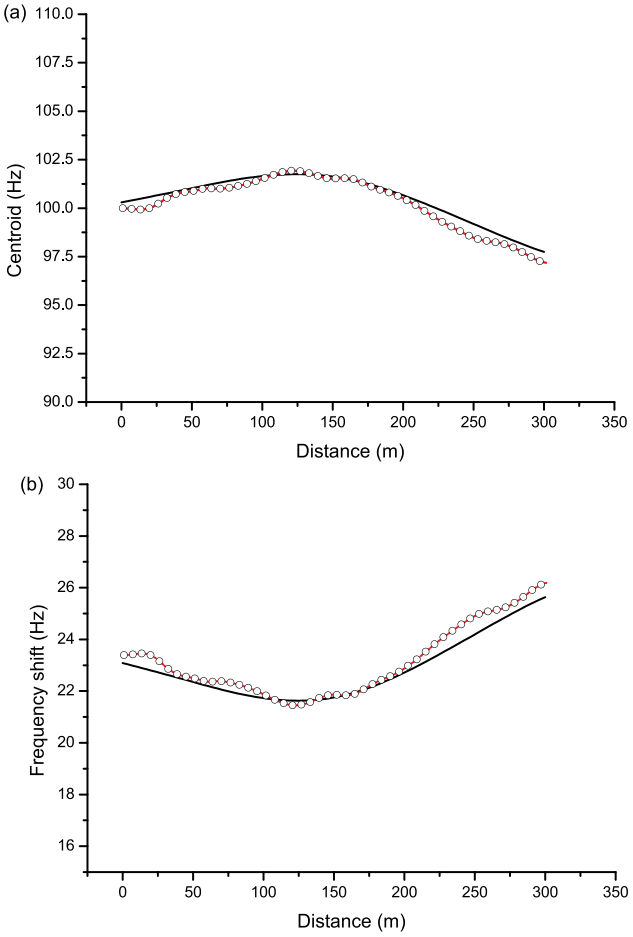

Figure 17. Centroids (a) and frequency shifts (b) at the receivers as a function of distance. The solid line and circles correspond to the 2-D theoretical (ray tracing) and numerical solutions, respectively. The medium is heterogeneous and the model is given in Fig. 14.

Alternative methods to the robust frequency-shift method include spectral ratio, rise time and amplitude decay, as well as the RMS approach. The spectral ratio and rise-time methods are sensitive to noise, whereas frequency shift, based on the peak frequency and, even better, the spectrum centroid, offers superior, localized estimates.

5 CONCLUSIONS

Battaglia and Aki's method for localizing seismic sources assumes a homogeneous 3-D medium with known velocities and quality factors or attenuations. It is based on the anelastic and geometric decay of the signal from the source to the receiver and uses an objective function defined as the RMS of the signal within a time window.

Here, we generalize the method to heterogeneous media by employing a ray tracing algorithm and redefining the objective function in terms of the centroid of the signal spectrum, rather than the signal amplitude as in the Battaglia–Aki method, which requires inversion for source strength. This inversion is unnecessary in our approach, as the centroid does not depend on source strength.

It can be shown that with a high signal-to-noise ratio and a well-defined signal, the peak frequency shift can be used, making the algorithm faster. However, when these conditions are not met, the centroid shift provides better results. The method is demonstrated in both 2-D and 3-D spaces, where the Green's functions are the Hankel and exponential functions, respectively. Average complex velocities and quality factors describing attenuation from the source to the receivers are obtained. The method assumes that the geometry and wave velocity of the layers are known (e.g. from traveltime tomography or migration). To localize the source, the quality factors must be known. If the source location is known, the quality factors of the layers can be determined.

Minimizations are performed using the Praxis algorithm and simulated annealing, and synthetic test seismograms are generated using a direct full-wave algorithm based on the Fourier pseudospectral method.

ACKNOWLEDGEMENT

We thank Luca de Siena for useful comments.

CONFLICT OF INTEREST

There are no conflicts to report and/or disclose.

DATA AVAILABILITY

The authors confirm that there is no data supporting the findings of this study. The software is not in the public domain, but it can be provided under a mutual agreement.

REFERENCES

Båth, M., 1979. *Introduction to Seismology,* Birkhäuser.

Battaglia, J. & Aki, K., 2003. Location of seismic events and eruptive fissures on the Piton de la Fournaise volcano using seismic amplitudes, *J. geophys. Res.,* **108**(B8), 2364.

Bazaraa, M.S., Sherali, H.D. & Shetty, C.M., 2006. *Nonlinear Programming - Theory and algorithms, 3rd edn,* Wiley.

Blias, E., 2012. Accurate interval Q-factor estimation from VSP data, *Geophysics,* **77,** WA149–WA156.

Brent, R.P., 1971. *Algorithms for finding zeros and extrema of functions without calculating derivatives, Report STAN-CS-71-198,* Stanford University. https://dblp.org/rec/phd/us/Brent71.html See also https://people.sc.fsu.edu/ jburkardt/f77_src/praxis/praxis.html.

Carcione, J.M., 1999. Staggered mesh for the anisotropic and viscoelastic wave equation, *Geophysics,* **64,** 1863–1866.

Carcione, J.M., 2022. *Wave Fields in Real Media. Theory and Numerical Simulation of Wave Propagation in Anisotropic, Anelastic, Porous and Electromagnetic Media, 4th edn,* Elsevier.

Carcione, J.M. & Picotti, S., 2006. P-Wave seismic attenuation by slow-wave diffusion: effects of inhomogeneous rock properties, *Geophysics,* **71,** O1–O8.

Carcione, J.M. & Ursin, B., 2016. On Fermat principle and Snell law in lossy anisotropic media, *Geophysics,* **3,** T107–T116.

Carcione, J.M., Kosloff, D. & Kosloff, R., 1988. Viscoacoustic wave propagation simulation in the Earth, *Geophysics,* **53,** 769–777.

Carcione, J.M., Cavallini, F., Gei, D. & Botelho, M.A.B., 2015. On the earthquake source numerical implementation in the seismic wave equation, *J. Earthquake Eng.,* **19,** 48–59.

Carcione, J.M., Gei, D., Picotti, S. & Botelho, M.A.B., 2021. On the instantaneous frequency and quality factor.*Geophys. J. Int.,* **227,** 735–745.

Carcione, J.M., Mainardi, F., Qadrouh, A.N., Alajmi, M. & Ba, J., 2024a, The rheological models of Becker, Scott Blair, Kolsky, Lomnitz and Jeffreys revisited, and implications for wave attenuation and velocity dispersion. *Surv. Geophys.,* **45,** 695–720.

Carcione, J.M., Mainardi, F., Qadrouh, A.N., Alajmi, M. & Ba, J., 2024b, *Q* A review, *Surv. Geophys.,* **45,** 1435–1458.

Cavallini, F., Carcione, J.M., Vidal de Ventós, D. & Engell-Sørensen, L., 2017. Low-frequency dispersion and attenuation in anisotropic partially saturated rocks, *Geophys. J. Int.,* **209**(3), 1572–1584.

Chen, Z., Chen, X., Wang, Y. & Li, J., 2014. Estimation of Q factors from reflection seismic data for a band-limited and stabilized inverse Q filter driven by an average-Q model, *J. Appl. Geophys.,* **101,** 86–94.

Corana, A., Marchesi, M., Martini, C. & Ridella, S., 1987. Minimizing multimodal functions of continuous variables with the simulated annealing algorithm, *ACM Trans. Math. Softw.,* **13,** 262–280.

Goffe, W.L., Ferrier, G.D. & Rogers, J., 1994. Global optimization of statistical functions with simulated annealing, *J. Econometrics,* **60**(1–2), 65–99. https://econwpa.ub.uni-muenchen.de/econ-wp/prog/papers/9406/9406001.txt.

Gradshteyn, I.S. & Ryzhik, I.M., 2007. *Table of Integrals, Series, and Products, 7th edn.,* Academic Press.

Kiefer, J., 1953. Sequential Minmax search for a maximum, *Proc. Am. Math. Soc.,* **4,** 502–506.

Kumagai, H. *et al.*, 2010. Broadband seismic monitoring of active volcanoes using deterministic and stochastic approaches, *J. geophys. Res.,* **115,** B08303.

Mainardi, F., 2022. *Fractional Calculus and Waves in Linear Viscoelasticity: An Introduction to Mathematical Models,* World Scientific.

Michelini, A. & McEvilly, T.V., 1991. Seismological studies at Park- field. I. Simultaneous inversion for velocity structure and hypocenters using cubic B-splines parameterization, *Bull. seism. Soc. Am.,* **81**(2), 24–552.

Onnis, L. & Carcione, J.M., 2017. A seismic ray-tracing method based on Fibonacci search, *Ann. Geophys.,* **60**.

Permana, T., Nishimura, T., Nakahara, H., Fujita, E. & Ueda, H., 2020. Reliability evaluation of volcanic tremor source location determination using cross-correlation functions, *Geophys.J. Internat.,* **220,** 1300–1315.

Picotti, S. & Carcione, J.M., 2006. Estimating seismic attenuation (Q) in the presence of random noise, *J. Seism. Exploration,* **15,** 165–181.

Qadrouh, A.N., Carcione, J.M., Alajmi, M. & Alyousif, M.M., 2019. A tutorial on machine learning with geophysical applications, *Boll. Geof. Teor. Appl.,* **60,** 375–402.

Qadrouh, A.N., Carcione, J.M., Ba, J., Gei, D. & Salim, A.M., 2017. Backus and Wyllie averages for attenuation, *Pure appl. Geophys.,* **175,** 165–170.

Quan, Y. & Harris, J.M., 1997. Seismic attenuation tomography using the frequency shift method, *Geophysics,* **62,** 895–905.

Robinson, E.A. & Treitel, S.. 1980. *Geophysical Signal Analysis,* Prentice-Hall Publishing, Tulsa, Ok.

Tonn, R., 1991. The determination of seismic quality factor *Q* from VSP data: a comparison of different computational methods, *Geophys. Prosp.,* **39,** 1–27.

Zeng, X. & West, G.F., 1996. Reducing spurious diffractions in elastic wavefield calculations, *Geophysics,* **61,** 1436–1439.

APPENDIX A: RAY TRACING

The source is located in the lower medium at (x_s, y_s) and a receiver at (x_r, y_r). The ray departs from the source up to the surface at an angle γ with respect to the vertical. Fig. 1 illustrates the transmission. On departure from the source, the ray is defined by two points: the source location (x_s, y_s) and $(x_s - y_s \tan\gamma, 0)$, a point at the surface. The ray intersects the interface finely discretized by 2000 segments and the intersection point is found. Rays outside the model are discarded. At the interface the Snell law is applied to compute the transmission angle. The incidence angle is $\theta = \gamma + \beta$, where β is the angle shown in Fig. 1. Then, the transmission angle to the

upper medium is θ', obtained from

$$\frac{\sin\theta}{v} = \frac{\sin\theta'}{v'} \quad \text{(Snell law)}, \tag{A1}$$

where v and v' are the phase velocities of the incidence and transmission media, respectively, which depend on frequency (e.g. J.M. Carcione 2022, section 3.5). The new angle of incidence to the next interface of the transmitted ray with respect to the vertical axis is the transmission angle $\gamma' = \theta' - \beta$. The process then continues in the same way up to the surface. The transmission coefficient, wave loss and geometric spreading along the rays are applied as shown in Section 3.

APPENDIX B: *R*–*T* COEFFICIENTS FOR STRESS AND DISPLACEMENT

Let us assume a 1-D acoustic medium and an incident stress wave on an interface separating the incidence and transmission media of impedance Z and Z', respectively. The incident, reflected and transmitted fields are

$$\begin{aligned} \sigma_{\rm I} &= \exp(-{\rm i}kz), \\ \sigma_{\rm R} &= R\exp(+{\rm i}kz), \\ \sigma_{\rm T} &= T\exp(-{\rm i}k'z), \end{aligned} \tag{B1}$$

where $k = \omega/v$, and we have omitted for simplicity the factor $\exp({\rm i}\omega t)$. The boundary conditions for a welded interface are

$$\begin{aligned} \sigma_{\rm I} + \sigma_{\rm R} &= \sigma_{\rm T}, \\ u_{\rm I} + u_{\rm R} &= u_{\rm T}, \end{aligned} \tag{B2}$$

where u denotes the displacement. Because $\sigma = \rho v^2 \partial_z u = \pm {\rm i}\omega Z u$, we have

$$u = \pm\frac{\sigma}{{\rm i}\omega Z}, \quad \text{(plus sign for the reflected wave)} \tag{B3}$$

For an interface at $z = 0$, we have from (B2),

$$1 + R = T, \quad \frac{1}{Z} - \frac{R}{Z} = \frac{T}{Z'}. \tag{B4}$$

Then,

$$R = \frac{Z' - Z}{Z + Z'}, \qquad T = \frac{2Z'}{Z + Z'} \tag{B5}$$

for stress. The second equation is a particular case of eq. (11). These coefficients must be taken into account when recording pressure (e.g. using hydrophones).

The energy balance gives

$$1 = R^2 + \mathcal{T}^2, \quad \mathcal{T}^2 = \frac{Z}{Z'}T^2, \tag{B6}$$

which is consistent with the first eq. (11).

On the other hand, assuming the expressions (B1) for the displacements and imposing the boundary conditions, we obtain

$$R_{\rm u} = \frac{Z - Z'}{Z + Z'}, \qquad T_{\rm u} = \frac{2Z}{Z + Z'} \tag{B7}$$

for displacement. These coefficients must be taken into account when recording displacement or particle velocity (e.g. using geophones).

APPENDIX C: INTERVAL-*Q* ESTIMATION FOR FLAT INTERFACES

The method assumes that the initial (source) spectrum is known (f_0), as well as the seismic velocities and location of the interfaces, that is, T_N can be computed. It requires only zero-offset transmission data, that is, frequency-shifts from each interface to the surface. Using eq. (20) or (22), $\bar{Q}_N$ can be obtained. If the source is located at interface j, we have from eq. (13),

$$\bar{Q}_j = T_j\left(\sum_{i=1}^{j}\frac{t_i}{Q_i}\right)^{-1}, \quad T_j = \sum_{i=1}^{j} t_i. \tag{C1}$$

From these equations we have

$$\frac{T_j}{\bar{Q}_j} = \sum_{i=1}^{j}\frac{t_i}{Q_i} = \frac{t_j}{Q_j} + \sum_{i=1}^{j-1}\frac{t_i}{Q_i} = \frac{t_j}{Q_j} + \frac{T_{j-1}}{\bar{Q}_{j-1}} = \frac{T_j - T_{j-1}}{Q_j} + \frac{T_{j-1}}{\bar{Q}_{j-1}}, \tag{C2}$$

which gives

$$Q_j = \frac{T_j - T_{j-1}}{T_j/\bar{Q}_j - T_{j-1}/\bar{Q}_{j-1}} \tag{C3}$$

R. Tonn (1991), E. Blias (2012), Z. Chen et al. (2014) and others have used this method.

APPENDIX D: SOURCE-LOCATION ALGORITHM

This approach is a generalization of the method of J. Battaglia & K. Aki (2003) to the heterogeneous case. We consider short-duration signals or transients at the receiver $r(t)$, such as earthquakes and direct seismic waves. J. Battaglia & K. Aki (2003, eq. 9) minimize the squared error between the expected and observed signals

$$\mathrm{Err}(x_s, y_s) = \sum_m (R^m - R^m_{\mathrm{obs}})^2, \tag{D1}$$

where m indicates the receiver, (x_s, y_s) is the source location, R^m is the RMS amplitude of the signal recorded at receiver m and R^m_{obs} is the observed RMS.

Instead, we use the centroid of the signal (7) and the objective function

$$O(x_s, y_s) = \sum_m \left[|\Delta f_m - \Delta f_m(\mathrm{obs})| + |T_{Nm} - T_{Nm}(\mathrm{obs})| \right], \tag{D2}$$

where Δf_m and T_{Nm} are the computed centroids shifts and traveltimes at the receivers (with index m), respectively, and $\Delta f(\mathrm{obs})$ and $T_N(\mathrm{obs})$ are the observed values. The integrals in eq. (7) are discretized in frequency.

APPENDIX E: FIBONACCI SEARCH ALGORITHM

The Fibonacci search method (J. Kiefer 1953) is a sequential search algorithm for minimizing an unimodal function over a closed interval, based on the Fibonacci numbers F_n defined as:

$$F_0 = F_1 = 1, \quad F_n = F_{n-1} + F_{n-2}, \quad n \geq 2. \tag{E1}$$

Unlike other sequential search methods (i.e. uniform, dichotomous, or the closely related golden section search method) Fibonacci search requires a pre-determined number of iterations. Its main advantage is that for the same starting uncertainty interval and number of iterations no other sequential search technique can result in a smaller final uncertainty interval.

Let $f(x)$ be the function to minimize, q the total number of iterations and $[a_m, b_m]$ the uncertainty interval after the m-th iteration. The algorithm prescribes the evaluation of the function at two interior points, c_m and d_m given by

$$\begin{aligned} c_m &= a_m + \frac{F_{q-m-1}}{F_{q-m+1}}(b_m - a_m) \\ d_m &= a_m + \frac{F_{q-m}}{F_{q-m+1}}(b_m - a_m) \qquad m = 1, \ldots, q-1. \end{aligned} \tag{E2}$$

If $f(c_m) > f(d_m)$ the uncertainty interval at the next iteration, $[a_{m+1}, b_{m+1}]$, will we $[c_m, b_m]$, otherwise if $f(c_m) \leq f(d_m)$, it is $[a_m, d_m]$. This is due to the function's unimodality. In both cases, it follows from eq. (E2) that the new interval length is

$$b_{m+1} - a_{m+1} = \frac{F_{q-m}}{F_{q-m+1}}(b_m - a_m). \tag{E3}$$

Additionally, it can be shown (e.g. M.S. Bazaraa et al. 2006, p. 351–353) that for the next iteration, either $c_{m+1} = d_m$ or $d_{m+1} = c_m$. Thus every iteration after the first requires only one function evaluation. After $q - 1$ iterations (and q function evaluations) the interval length is

$$b_{q-1} - a_{q-1} = \frac{b_1 - a_1}{F_q}. \tag{E4}$$

For the very last evaluation, eq. (E2) yields $c_{q-1} = d_{q-1}$, both in the centre of interval $[a_{q-1}, b_{q-1}]$. In order to distinguish them, one of them is slightly displaced. Taking $d_{q-1} = c_{q-1} + \epsilon$, with ϵ very small, it is possible to reduce the final interval length by approximately 1/2, obtaining

$$b_q - a_q = \frac{b_1 - a_1}{2F_q} \tag{E5}$$

The total number of iterations must be selected *a priori*, taking eq. (E5) into account to achieve the desired accuracy level.

APPENDIX F: FULL-WAVE MODELLING METHOD

The full-wave synthetic seismograms are computed with a modelling code based on the viscoacoustic stress–strain relation corresponding to multiple relaxation mechanisms, based on L Zener elements. The equations for viscoelastic media are given in section 3.9 of J.M. Carcione (2022). The 2-D particle velocity-stress formulation for viscoacoustic media is

$$\begin{aligned}
\dot{v}_x &= \frac{1}{\rho}\partial_x\sigma + f_x,\\
\dot{v}_z &= \frac{1}{\rho}\partial_z\sigma + f_z,\\
\dot{\sigma} &= \rho v^2\left(\vartheta + \textstyle\sum_l^L e_l\right) + \dot{s},\\
\dot{e}_l &= \frac{1}{\tau_{\sigma l}}\left(\sum_{l=1}^{L}\frac{\tau_{\epsilon l}}{\tau_{\sigma l}}\right)^{-1}\left(1-\frac{\tau_{\epsilon l}}{\tau_{\sigma l}}\right)\vartheta - \frac{e_l}{\tau_{\sigma l}},\\
\vartheta &= \partial_x v_x + \partial_z v_z
\end{aligned} \tag{F1}$$

where $v_{(.)}$ is particle velocity, $\sigma_{(.)}$ is stress, f_i are directional forces, s is the source (explosion), e_l are memory variables and the τ denote relaxation times. Omitting the indices, these are given by

$$\tau_\epsilon = \frac{\tau_0}{Q_0}\left(\sqrt{Q_0^2+1}+1\right) \quad \text{and} \quad \tau_\sigma = \frac{\tau_0}{Q_0}\left(\sqrt{Q_0^2+1}-1\right), \tag{F2}$$

where Q_0 is a minimum quality factor and τ_0 is defined as follows. If f_0 is the central frequency of the source wavelet, we assume that the middle relaxation peak is located at $\omega_0 = 1/\tau_0 = 2\pi f_0$. The velocity v in these equations corresponds to the unrelaxed or high-frequency limit velocity.

The numerical algorithm is based on the Fourier pseudo-spectral method for computing the spatial derivatives and a fourth-order Runge–Kutta technique for calculating the wavefield recursively in time (e.g. J.M. Carcione 2022, sections 9.3.2 and 9.2.3).

Eliminating the particle velocities and setting $f_x = f_z = 0$, eqs (F1) can be written as

$$\ddot{\sigma} = v^2\left(\Delta\sigma + \rho\sum_l^L \dot{e}_l\right) + \ddot{s}. \tag{F3}$$

The complex modulus and complex velocity are

$$M = \rho v^2\left(\sum_{l=1}^{L}\frac{\tau_{\epsilon l}}{\tau_{\sigma l}}\right)^{-1}\sum_l^L\frac{1+\mathrm{i}\omega\tau_{\epsilon l}}{1+\mathrm{i}\omega\tau_{\sigma l}} \tag{F4}$$

$$v_c = \sqrt{\frac{M}{\rho}}, \tag{F5}$$

(J.M. Carcione 2022, eqs 2.224 and 2.83), respectively.